RSC Advances

PAPER

Cite this: *RSC Adv.*, 2018, **8**, 42308

Large enhanced photocatalytic activity of g-C_3N_4 by fabrication of a nanocomposite with introducing upconversion nanocrystal and Ag nanoparticles†

Feifei Zhao,‡ Kyu Kyu Khaing,‡ Dongguang Yin,* Bingqi Liu, Tao Chen, Chenglong Wu, Kexian Huang, LinLin Deng and Luqiu Li

Received 23rd September 2018
Accepted 29th November 2018

DOI: 10.1039/c8ra07901c

rsc.li/rsc-advances

A novel heterostructured nanocomposite UCNPs@SiO_2@Ag/g-C_3N_4 was developed for the first time to substantially boost the solar-light driven photocatalytic activity of g-C_3N_4. Its photocatalytic properties and photocatalytic mechanism were investigated. The as-synthesized photocatalyst with excellent improvement in the solar absorption and separation efficiency of photoinduced electron–hole pairs exhibited optimum solar-induced photocatalytic activity in dye degradation and hydrogen production. The experimental results showed that the rates of degradation of Rhodamine B (RhB) and hydrogen evolution were about 10 and 12 times higher than that of pristine g-C_3N_4, respectively. The excellent photocatalytic activity was attributed to the synergetic effect of upconversion nanoparticles (UCNPs) and Ag nanoparticles (NPs) on the modification of the photocatalytic properties of g-C_3N_4, resulting in a broad light response range for g-C_3N_4 as well as the fast separation and slow recombination of photoinduced electron–hole pairs. This study provides new insight into the fabrication of g-C_3N_4-based nanocomposite photocatalysts with high catalytic efficiency through the artful assembly of UCNPs, Ag NPs and g-C_3N_4 into a hetero-composite nanostructure. The prominent improvement in photocatalytic activity enables the potential application of g-C_3N_4 in the photocatalytic degradation of organic pollutants and hydrogen production utilizing solar energy.

1. Introduction

In recent years, the energy crisis and the continued deterioration of the global environment have become serious problems that have attracted great attention all over the world.[1,2] Semiconductor-based photocatalysis is a potential strategy for solving these problems through photocatalytic water splitting to produce clean energy hydrogen and the degradation of organic pollutants using solar energy.[3–5] Semiconductor photocatalysts with low toxicity, good stability, and high activity under solar light are essential for practical photocatalytic applications.[6] However, the most widely used and representative semiconductor photocatalysts, such as TiO_2 and ZnO, can only respond to UV light with low quantum efficiency under solar light irradiation, which greatly limits their practical applications using solar energy.[7] Therefore, the development of new visible light response photocatalysts with high quantum efficiency has become a hot issue in the field of photocatalysis.

Recently, as a metal-free polymeric semiconductor, graphitic carbon nitride (g-C_3N_4) has gained extensive attention owing to its outstanding merits such as visible-light response, Earth-abundance, high chemical and thermal stabilities, and suitable valence and conduction band potentials for producing hydrogen and oxygen by photocatalytic water splitting.[8,9] These unique properties make g-C_3N_4 a promising photocatalyst for photocatalytic hydrogen production and the degradation of organic pollutants using solar energy. However, it has been found that g-C_3N_4 suffers from narrow visible-light response range, fast charge recombination, and small specific surface area, which limit its practical applications.[10–12] To date, various strategies have been developed, such as morphology modification, coupling with other semiconductors to form nanoheterojunctions, doping of metal and/or nonmetal ions, and copolymerization with other kinds of π-conjugated organic molecules.[13–17] Although the photocatalytic activity of g-C_3N_4 has been improved to varying degrees by the above strategies, the obtained g-C_3N_4-based photocatalysts still cannot satisfy the needs of the practical applications with respect to photocatalytic activity under solar light irradiation.

In order to utilize solar energy, most strategies in previous studies have focused on extending the optical response range of g-C_3N_4 into the visible region.[6,17–19] Nonetheless, having photocatalysts that respond only to visible light, with the near-

School of Environmental and Chemical Engineering, Shanghai University, Shanghai, 200444, China. E-mail: ydg@shu.edu.cn

† Electronic supplementary information (ESI) available. See DOI: 10.1039/c8ra07901c

‡ Feifei Zhao and Kyu Kyu Khaing are co-first authors.

infrared (NIR) light being wasted, is far from satisfactory. It is well-known that the NIR light accounts for a large proportion (~46%) of the whole solar energy.[20] Moreover, electron–hole pairs that are photo-generated by the excitation of visible light usually possess low oxidation–reduction potentials.[7,20,21] Only those electron–hole pairs produced from the excitation of ultraviolet light possess high oxidation and reduction capabilities to completely degrade pollutants.[22,23] In view of these, the combination of semiconductors with rare earth UCNPs is a facile and efficient method to substantially utilize the solar energy and improve the photocatalytic activity of semiconductor photocatalysts.[24,25] The UCNPs can convert two or more NIR photons with lower energy into UV and visible emission,[26] which can subsequently be absorbed by the semiconductor. This enables the indirect utilization of the NIR photons for photocatalysis. Moreover, the high-energy UV light from the UCNPs can excite the semiconductor to generate electron–hole pairs with high oxidation–reduction potentials. There have been reports, including ours, on the combination of UCNPs with some inorganic semiconductors such as TiO_2 and CeO_2.[27,28] It has been proved that this strategy is effective for improving the photocatalytic activity of semiconductor photocatalysts.[25] However, there are few reports about the coupling of UCNPs with g-C_3N_4. Furthermore, these inorganic semiconductors have inflexible band structures, and they can hinder light absorption due to serious light scattering, but g-C_3N_4 has a readily tunable energy band and highly transparent morphology.[27,28] Thus, a combination of g-C_3N_4 with UCNPs is likely to make better use of the upconversion energy from NIR light and subsequently improve the photocatalytic performances of g-C_3N_4 more efficiently.

Plasmonic metallic nanostructures, for example, Ag NPs, combined with semiconductor photocatalysts for achieving high-efficiency photocatalysis by the efficient separation of charge carriers have been reported.[17,29,30] In this study, in view of combining g-C_3N_4 with UCNPs and Ag NPs for the substantial utilization of solar energy as well as restraining the recombination rate of photo-generated electrons and holes, we designed and synthesized a novel g-C_3N_4-based nanocomposite photocatalyst UCNPs@SiO_2@Ag/g-C_3N_4. We first prepared a sandwich-structure nanocomposite of UCNPs@SiO_2@Ag and then loaded this nanocomposite onto the surface of g-C_3N_4 to form the final product. Taking advantage of the synergistic effect from UCNPs and Ag NPs, the nanocomposite photocatalyst shows very high photocatalytic efficiency for dye degradation and hydrogen evolution under solar light irradiation, demonstrating that the designed strategy can significantly improve the photocatalytic activity of g-C_3N_4 under solar light irradiation.

2. Experimental section

2.1. Materials

Rare-earth oxides Lu_2O_3 (99.999%), Gd_2O_3 (99.999%), Yb_2O_3 (99.999%), and Tm_2O_3 (99.999%) were purchased from Shanghai Yuelong New Materials Co. Ltd. Oleic acid (OA; >90%), 1-octadecene (ODE; >90%), CO-520, tetraethylorthosilicate (TEOS; >99%), 1,4-benzoquinone (BQ), disodium ethylenediaminetetraacetate (Na_2EDTA), *tert*-butyl alcohol (*t*-BuOH), and Rhodamine B (RhB) were purchased from Sigma-Aldrich. Trifluoroacetic acid (99.0%), (3-aminopropyl)triethoxysilane (APTES; >98%), $NH_3 \cdot H_2O$ (28 wt%), ethanol, cyclohexane, acetone, sodium carbonate, silver nitrate, sodium citrate, and urea were purchased from Sinopharm Chemical Reagent Co. Ltd. (Shanghai). $Ln(CF_3COO)_3$ (Ln: Lu, Gd, Yb, and Tm) precursors were prepared by dissolving the corresponding metal oxides in trifluoroacetic acid at elevated temperature. Milli-Q water was used in the experiments. All other chemical reagents were of analytical grade and were used without further purification.

2.2. Synthesis

2.2.1. Preparation of g-C_3N_4. Bulk g-C_3N_4 powder was synthesized according to the procedure described in a previous paper.[31] In detail, urea (40 g) was placed into a covered alumina crucible and then heated in a muffle furnace with a ramp rate of 5 °C min^{-1} to 600 °C, and maintained at the target temperature for 4 h in static air. After being naturally cooled to room temperature, the yellow powder was collected and milled into powder in a mortar.

The nanosheets of g-C_3N_4 were prepared by thermal oxidation etching of the bulk g-C_3N_4 obtained as above in static air as follows:[32] 400 mg of the bulk g-C_3N_4 was placed in an open ceramic container and was heated at 500 °C for 2 h with a ramp rate of 5 °C min^{-1}. A light yellow powder of g-C_3N_4 nanosheets was finally obtained.

2.2.2. Preparation of $NaLuF_4$:Gd,Yb,Tm. The $NaLuF_4$:Gd,Yb,Tm nanoparticles were prepared using a method similar to our previous report with slight modifications.[33] Typically, 2 mmol of CF_3COONa, 0.555 mmol of $Lu(CF_3COO)_3$, 0.24 mmol of $Gd(CF_3COO)_3$, 0.2 mmol of $Yb(CF_3COO)_3$ and 0.005 mmol of $Tm(CF_3COO)_3$ were added to a mixture of OA (6 mL) and ODE (6 mL) in a three-necked flask at room temperature. The solution was pre-degassed for 30 min with vigorous magnetic stirring and then heated to 110 °C under vacuum for 30 min to remove water and oxygen. The resulting solution was heated to 325 °C at a rate of ~15 °C min^{-1} and maintained for 1 h under argon protection. After naturally cooling down to room temperature, an excess amount of ethanol was added to the solution. The resultant mixture was centrifuged at 8000 rpm for 15 min and washed with ethanol–cyclohexane (4 : 1, v/v) three times. The collected precipitate was dispersed in cyclohexane.

2.2.3. Synthesis of $NaLuF_4$:Gd,Yb,Tm@$NaLuF_4$:Gd,Yb. CF_3COONa (1 mmol), 0.5 mmol $Ln(CF_3COO)_3$ (Ln: 66% Lu, 24% Gd, 10% Yb), and the prepared $NaLuF_4$:Gd,Yb,Tm nanocrystals (1 mmol) were added to a mixture of OA (6 mL) and ODE (6 mL) in a three-necked flask at room temperature. The solution was pre-degassed for 30 min with vigorous magnetic stirring and then heated to 110 °C under vacuum for 30 min to remove water and oxygen. The resulting solution was heated to 325 °C at a rate of ~15 °C min^{-1} and maintained for 1 h under argon protection. After naturally cooling down to room temperature, an excess amount of ethanol was poured into the solution. The resultant mixture was centrifuged at 8000 rpm for 15 min and

washed with ethanol–cyclohexane (4 : 1, v/v) three times. The collected precipitate was dispersed in cyclohexane.

2.2.4. Preparation of UCNPs@SiO_2. CO-520 (0.1 mL), cyclohexane (6 mL), and 25 mM $NaLuF_4$:Gd,Yb,Tm@$NaLuF_4$:Gd,Yb nanocrystals solution in cyclohexane (4 mL) were mixed and stirred for 10 min, then 0.4 mL of CO-520 and 0.08 mL of 28 wt% $NH_3 \cdot H_2O$ were added and the container was sealed and sonicated for 20 min until a transparent emulsion was formed. TEOS (0.08 mL) was then added to the solution followed by stirring for 48 h at a speed of 600 rpm. After adding a definite amount of acetone, the UCNPs@SiO_2 nanoparticles were precipitated. The obtained precipitate was washed with ethanol/water (1 : 1 v/v) twice and then re-dispersed in ethanol.

2.2.5. Preparation of UCNPs@SiO_2@Ag. The UCNPs@SiO_2 nanoparticles obtained above were dispersed in 10 mL ethanol with ultrasonic stirring for 30 min. APTES (0.13 mL) was then added to the mixture and magnetic stirring was continued for 10 min. Subsequently, a certain amount of $AgNO_3$ dispersed in 10 mL deionized water was added to the mixture with magnetic stirring, and the stirring was maintained for 20 min. A certain amount of sodium citrate was then added to the mixture and the temperature was increased to 100 °C and maintained for 20 min. After cooling the mixture to room temperature, the obtained UCNPs@SiO_2@Ag nanoparticles were separated by centrifugation and washed three times with ethanol/water (1 : 1 v/v). The final product was dispersed in ethanol.

2.2.6. Preparation of UCNPs@SiO_2@Ag/g-C_3N_4. The UCNPs@SiO_2@Ag nanoparticles obtained above were dispersed in 10 mL of ethanol by sonication. Then, 34 mg of g-C_3N_4 dispersed in 20 mL of deionized water was added to the solution with magnetic stirring and the stirring was maintained for 12 h at room temperature. The obtained suspension was transferred into a Teflon-lined stainless steel autoclave and heated at 180 °C for 24 h in an electric oven. After the reaction, the product was collected by centrifugation, followed by washing with deionized water and ethanol three times. Finally, the production was dried under vacuum at 80 °C overnight.

Based on the procedures in 2.2.5 and 2.2.6, the UCNPs@SiO_2@Ag/g-C_3N_4 photocatalysts with different loading levels of Ag NPs were prepared by adding different amounts of $AgNO_3$ and sodium citrate. The obtained samples were marked as UCNPs@SiO_2@*X*wt%Ag/g-C_3N_4, with *X* representing the weight percentage of Ag relative to g-C_3N_4 in the nanocomposite and *X* varied from 0 to 10 ($X = 0$, 1, 3, 5, and 10).

2.2.7. Preparation of 3 wt%Ag/g-C_3N_4. $AgNO_3$ (1.61 mg) was dissolved in 10 mL deionized water with magnetic stirring for 20 min, then 1.83 mg of sodium citrate was added to the solution followed by heating to 100 °C and the temperature was maintained for 20 min. After cooling the solution to room temperature, the obtained Ag NPs were separated by centrifugation and washed three times with ethanol/water (1 : 1 v/v). The final product was dispersed in 10 mL ethanol, then 34 mg of g-C_3N_4 dispersed in 20 mL deionized water was added to the solution and magnetic stirring was continued for 12 h at room temperature. The as-obtained Ag/g-C_3N_4 suspension was transferred into a Teflon-lined stainless steel autoclave and heated at 180 °C for 24 h in an electric oven. After the reaction, the product was collected by centrifugation, followed by washing with deionized water and ethanol three times. Finally, the product was dried in vacuum at 80 °C overnight.

2.3. Characterization

The sizes and morphologies of the prepared products were characterized using a JEOL JEM-2010F transmission electron microscope (TEM) operating at 200 kV, equipped with an energy-dispersive X-ray (EDX) spectrometer. The powder X-ray diffraction (XRD) patterns were recorded by a Rigaku D/max-2500 X-ray diffractometer using Cu-Kα radiation. The 2θ angle of the XRD spectra was recorded at a scanning rate of 6 deg min^{-1} and was then converted to Cu-Kα radiation values using Bragg's law. The upconversion photoluminescence emission spectra were measured using an Edinburgh Instruments FLS920 fluorescence spectrophotometer. The samples were excited by a 980 nm continuous wave laser under the power density of 2 W cm^{-2}. UV-Vis absorption spectra were obtained on a Hitachi 3010 UV-Vis spectrophotometer (Hitachi, Japan). UV-Vis-NIR diffuse reflectance spectra (DRS) were obtained on a Shimadzu UV-3600 spectrometer by using $BaSO_4$ as a reference. Photoluminescence (PL) spectra were recorded by using an F-4500 fluorescence spectrophotometer with an excitation wavelength of 330 nm at room temperature.

2.4. Photocatalytic degradation of RhB and the detection of active species

Photocatalysis was performed *via* monitoring RhB degradation by measuring the variation of the optical absorption of RhB with a Hitachi U-3010 spectrophotometer using an SGY-IB multifunction photochemical reactor (Nanjing Sidongke Electric Co. Ltd) as the photocatalytic reaction device. In a typical experiment, 20 mg of catalyst was dispersed in a quartz cuvette containing 50 mL of RhB aqueous solution (20 mg L^{-1}). The suspension was magnetically stirred in the dark for 30 min to attain adsorption–desorption equilibrium between dye and catalyst. The photoreaction vessels were then exposed to the simulated solar light irradiation produced by a 300 W Xe lamp (PL-X500D) with a wavelength distribution similar to solar light. At given time intervals, the photoreacted solutions were analyzed by recording the variation in the absorption band maximum (554 nm) in the UV-Vis spectra of RhB.

2.5. Photocatalytic hydrogen evolution

Photocatalytic hydrogen generation reactions were conducted in an outer Pyrex irradiation cell connected to a closed gas circulation system. In a typical experiment, 20 mg of the photocatalyst powder was dispersed in 100 mL of aqueous solution containing 10 vol% triethanolamine (TEOA) as a scavenger. The deposition of 3 wt% Pt as a reducing co-catalyst was achieved by dissolving H_2PtCl_6 in the above 100 mL reaction solution. Before the reaction, the system was thoroughly vacuumed and nitrogen was introduced. The reaction temperature was kept at around 10 °C. The photocatalytic reactions were initiated by using a 300 W Xe-lamp (PLS-SXE300). The amount of H_2 generated was analyzed by online GC7900 gas chromatography.

2.6. Electrochemical and photoelectrochemical measurements

The photocurrents were measured by using an electrochemical workstation (CHI660A, Chen Hua Instruments, Shanghai, China) in a standard three-electrode system, which employed a platinum wire as the counter electrode, Ag/AgCl as the reference electrode, and the as-prepared photocatalysts served as working electrodes. The photocurrent intensity of the photocatalysis was measured at 0.0 V with the light on and off. Na_2SO_4 (0.1 M) was used as the supporting electrolyte for photocurrent measurements. A 300 W Xe lamp was utilized as a light source. The Nyquist plots were determined over the frequency range of 100–10^6 Hz with an ac amplitude of 10 mV at the open circuit.

3. Results and discussion

The fabrication of the nanocomposite photocatalyst is depicted in Scheme 1. The UCNPs of $NaLuF_4$:Gd,Yb,Tm@$NaLuF_4$:Gd,Yb were first synthesized through a thermal decomposition method.[33] A layer of amorphous SiO_2 as the media shell was generated outside the UCNPs *via* a reverse microemulsion method.[34] Ag NPs generated by the reduction of $AgNO_3$ using sodium citrate as the reductant were immobilized on the surface of the SiO_2 shell through a chemical affinity towards primary amines.[35] The primary amine originally acted as a ligand coming from APTES, which was introduced during the synthetic process. The obtained composite nanoparticles of UCNPs@SiO_2@Ag were immobilized on the surface of g-C_3N_4 through a hydrothermal treatment process to obtain the final product of the nanocomposite photocatalyst UCNPs@SiO_2@Ag/g-C_3N_4.

3.1. Structural and morphological characterization

The UCNPs@SiO_2@*X*wt%Ag/g-C_3N_4 (X = 0, 1, 3, 5, and 10) photocatalysts were characterized by various instruments. All of the samples show a similar structure and morphology. Herein, the UCNPs@SiO_2@3wt%Ag/g-C_3N_4 sample is used as an example to demonstrate the typical microstructure and morphology. The content of the Ag used in the sample for all studies, such as optical properties, structural and morphological, and photocatalytic, is the same as that of the 3 wt%.

As shown in Fig. 1a and b, both bulk g-C_3N_4 and g-C_3N_4 nanosheets display wrinkled laminar morphologies. The size of the bulk g-C_3N_4 is several micrometers (Fig. 1a), while the g-C_3N_4 nanosheets have average diameters in the submicrometer and/or nanometer range (Fig. 1b). As shown in Fig. 1c and d, both the core UCNPs ($NaLuF_4$:Gd,Yb,Tm) and core–shell UCNPs ($NaLuF_4$:Gd,Yb,Tm@$NaLuF_4$:Gd,Yb) are all hexagonal-phase crystals, with relatively uniform morphologies and sizes. The average diameters of the core and core–shell nanocrystals are 48 and 68 nm, respectively. Fig. 1e and f show that a light and smooth layer of SiO_2 with thickness of about 10 nm is coated around the UCNPs to form UCNPs@SiO_2 nanoparticles with uniform morphologies and sizes (Fig. 1e), and Ag NPs (about 6 nm) are attached to the surface of UCNPs@SiO_2 to form UCNPs@SiO_2@Ag nanoparticles (Fig. 1f). For the UCNPs@SiO_2@Ag/g-C_3N_4 sample, the g-C_3N_4 nanosheets serve as a catalyst and the support of the UCNPs@SiO_2@Ag nanoparticles. The UCNPs@SiO_2@Ag nanoparticles retain their initial morphology after being immobilized on the surface of the g-C_3N_4 nanosheets. As shown in Fig. 1g, all of the UCNPs@SiO_2@Ag nanoparticles are anchored to the g-C_3N_4 nanosheets, and no unanchored nanoparticles are observed. The HRTEM images of $NaLuF_4$:Gd,Yb,Tm@$NaLuF_4$:Gd,Yb and Ag NPs reveal the highly crystalline nature of the as-prepared products (Fig. 1h). The determined values of interplanar distances between adjacent lattice fringes are 0.50 and 0.224 nm, corresponding to (100) and (111) crystal planes of UCNPs and Ag nanoparticles,[27] respectively. The measured lattice space (0.50 nm) of UCNPs in UCNPs@SiO_2@Ag, corresponding to the (100) hexagonal phase crystal plane of UCNPs, demonstrates that the hexagonal phase structure of UCNPs remains unchanged after forming UCNPs@SiO_2@Ag nanoparticles. EDX spectroscopy was applied to confirm the chemical composition of the as-prepared samples. As shown in Fig. 2, all of the elements including C, N, Si, O, Na, F, Lu, Gd, Yb, Ag, and Tm were detected in UCNPs@SiO_2@Ag/g-C_3N_4, indicating that the exact ingredients were desirably built into the product. The elemental analysis of EDX mapping was further employed to identify the internal structure of UCNPs@SiO_2@Ag/g-C_3N_4. It can be seen from Fig. 2b–l that the elements of C and N are distributed homogeneously in the nanosheet, while the elements of Na, F, Lu, Gd, and Yb are mainly distributed in the

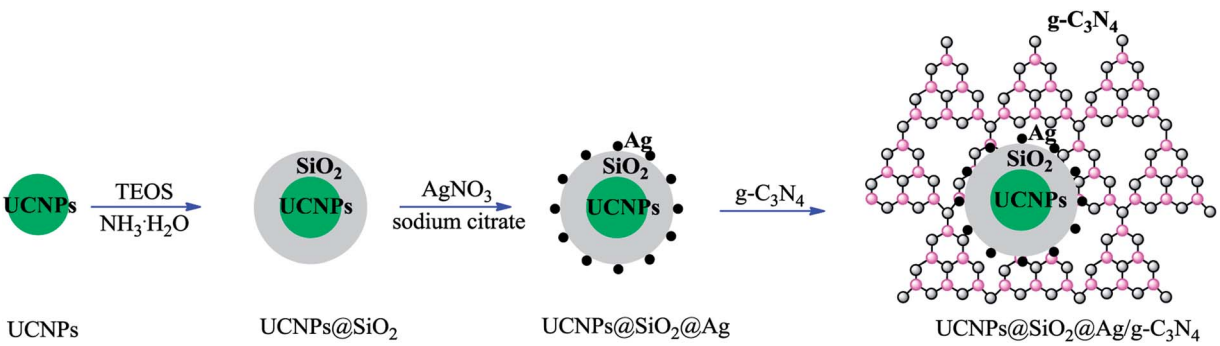

Scheme 1 Schematic of the fabrication process of the UCNPs@SiO_2@Ag/g-C_3N_4 photocatalyst.

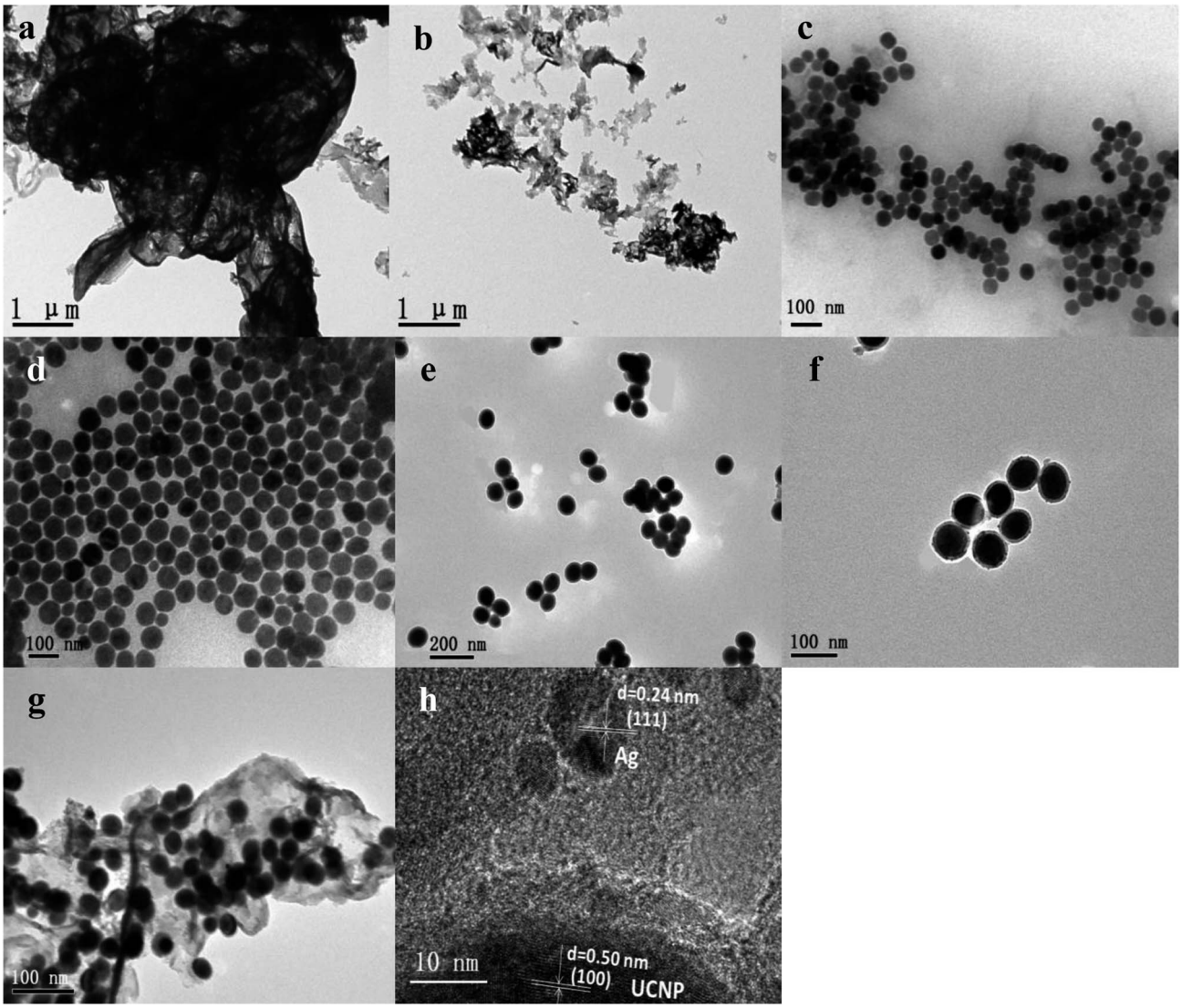

Fig. 1 TEM images of (a) bulk g-C_3N_4, (b) g-C_3N_4 nanosheets, (c) $NaLuF_4$:Gd,Yb,Tm, (d) $NaLuF_4$:Gd,Yb,Tm@$NaLuF_4$:Gd,Yb, (e) UCNPs@SiO_2, (f) UCNPs@SiO_2@Ag, (g) UCNPs@SiO_2@Ag/g-C_3N_4. (h) HRTEM image of UCNPs@SiO_2@Ag/g-C_3N_4.

core–shell UCNPs ($NaLuF_4$:Gd,Yb,Tm@$NaLuF_4$:Gd,Yb). The elements of Si, O and Ag are mainly distributed in the outermost shell of $NaLuF_4$:Gd,Yb,Tm@$NaLuF_4$:Gd,Yb@SiO_2, while the Tm is mainly distributed in the core. These results confirm the formation of core–shell–shell sandwich-structure nanoparticles of $NaLuF_4$:Gd,Yb,Tm@$NaLuF_4$:Gd,Yb@SiO_2 and the final nanocomposite catalyst of $NaLuF_4$:Gd,Yb,Tm@$NaLuF_4$:Gd,Yb@SiO_2@Ag/g-C_3N_4.

The crystal structures of the as-prepared samples were analyzed by XRD (Fig. 3). In the XRD pattern of g-C_3N_4, there are two prominent peaks at 13.1° and 27.4°, suggesting the presence of the phase pure g-C_3N_4 layered structure.[36] The peak at 13.1° for the (100) diffraction plane and 27.4° for the (002) diffraction plane were derived from the in-plane structural packing of tri-*s*-triazine units and interplanar stacking of conjugated aromatic systems, respectively.[25] The diffraction peak of the g-C_3N_4 at 27.4° also appeared in the UCNPs@SiO_2/g-C_3N_4 (Fig. S1 in ESI†) and UCNPs@SiO_2@Ag/g-C_3N_4 samples, indicating that the interplanar stacking structure of the g-C_3N_4 remained unchanged after it coupled with UCNPs. The samples of UCNPs, UCNPs@SiO_2/g-C_3N_4, and UCNPs@SiO_2@Ag/g-C_3N_4 show multiple characteristic diffraction peaks (100, 110, 101, 111, 200, 210, 002, 211, 112), which match well with the standard of β-$NaLuF_4$ (JCPDS 27-0726).[37] Both Ag/g-C_3N_4 and UCNPs@SiO_2@Ag/g-C_3N_4 show a typical face-centered cubic phase of silver (JCDS 04-0783),[38] confirming the formation of Ag NPs. All of the XRD results are in good agreement with the measured TEM results.

3.2. Optical properties

The photocatalytic activity of the photocatalysts is closely related to their light absorption ability and response range. For comparison of the optical properties, the UV-Vis-NIR diffuse reflectance spectra (DRS) of solid g-C_3N_4, 3 wt%Ag/g-C_3N_4, UCNPs@SiO_2/g-C_3N_4, and UCNPs@SiO_2@3wt%Ag/g-C_3N_4 were measured and shown in Fig. 4a. The g-C_3N_4 showed a strong

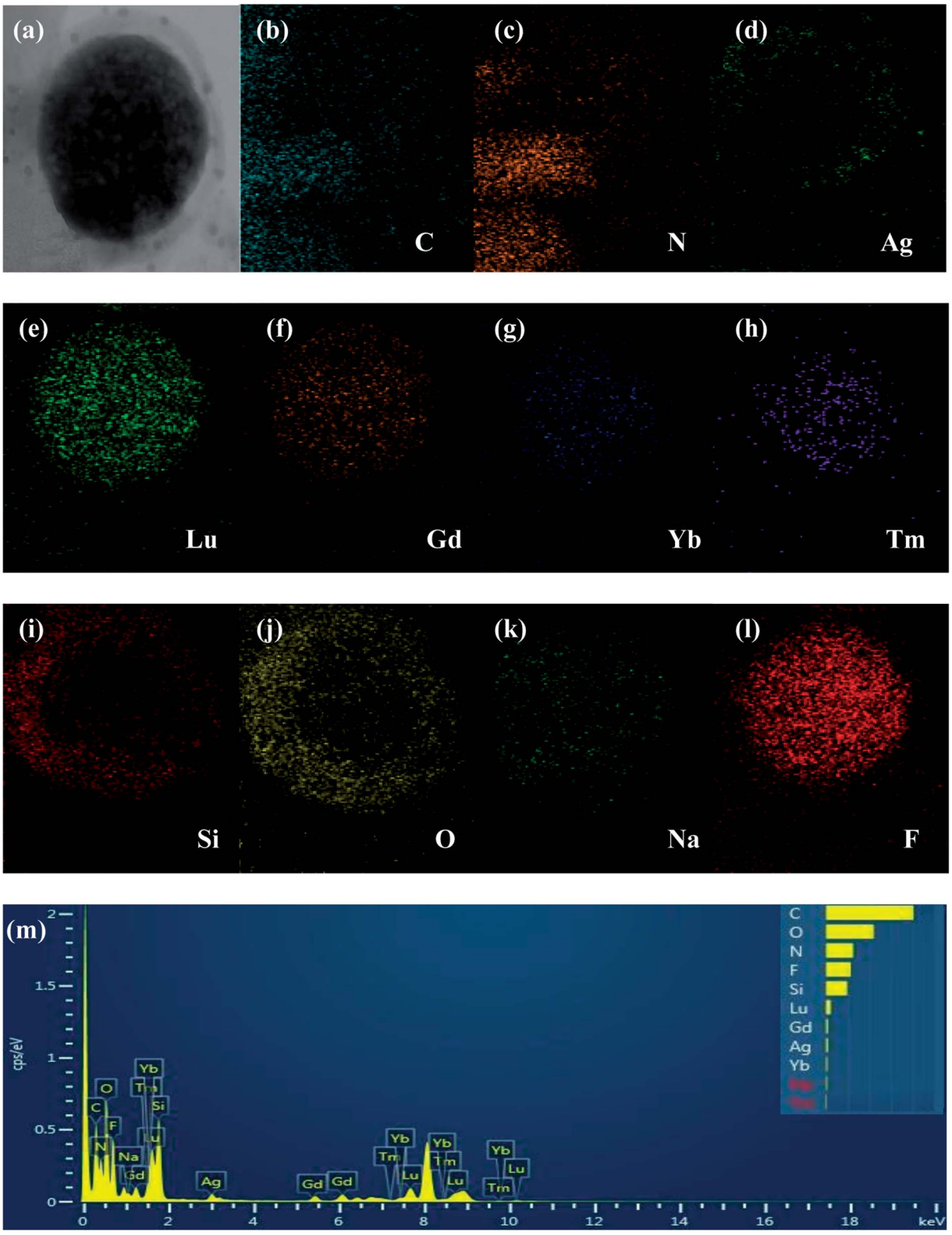

Fig. 2 (a–l) EDX elemental mapping images and (m) EDX spectroscopy of UCNPs@SiO_2@Ag/g-C_3N_4.

intrinsic absorption band from the UV to the visible range with an absorption edge at 460 nm, which was caused by the excitation of electrons from the valence band to the conduction band of g-C_3N_4.[10] The UCNPs@SiO_2/g-C_3N_4 exhibited a comparative low absorption and a blue-shifted absorption edge relative to the g-C_3N_4. The low absorption can be assigned to the multiple light scattering effects and shielding effect caused by the silica layer and UCNPs.[39] The blue-shifted

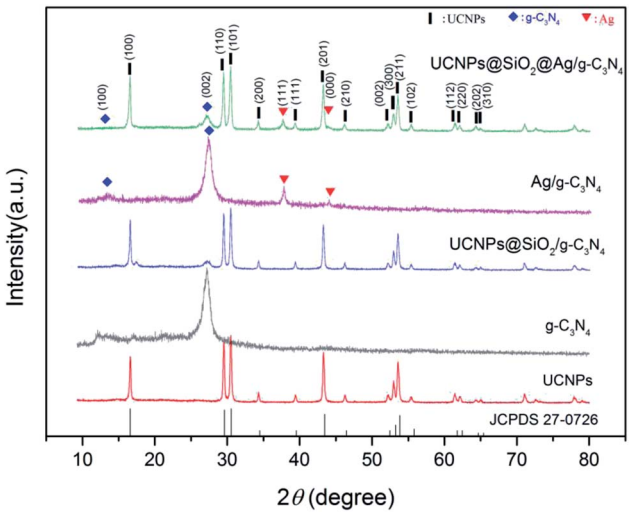

Fig. 3 XRD patterns of the as-prepared UCNPs ($NaLuF_4$:Gd,Yb,Tm@$NaLuF_4$:Gd,Yb), g-C_3N_4, UCNPs@SiO_2/g-C_3N_4, Ag/g-C_3N_4, and UCNPs@SiO_2@Ag/g-C_3N_4 samples. The corresponding standard data for the β-$NaLuF_4$ phase (JCPDS 27-0726) is also given at the bottom.

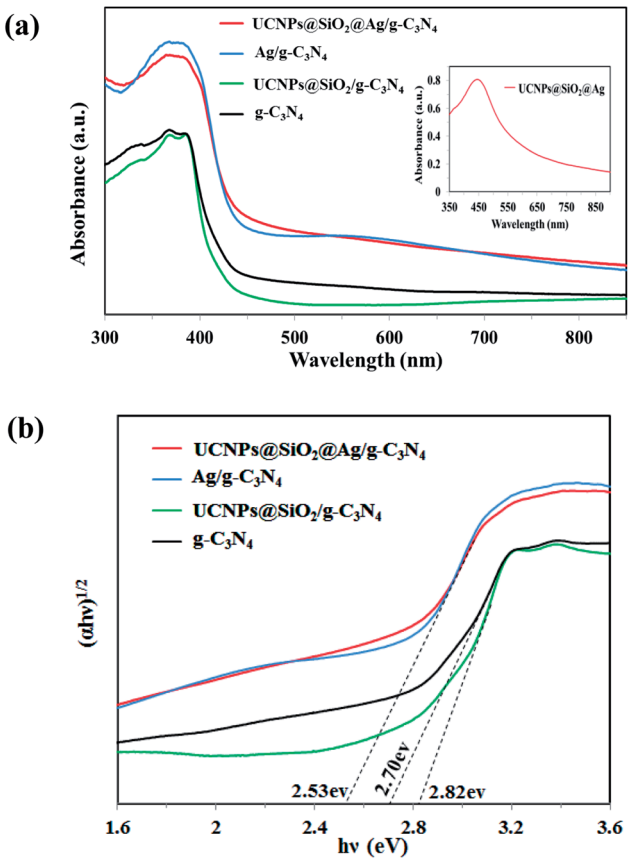

Fig. 4 (a) UV-Vis-NIR diffuse reflectance spectra of g-C_3N_4, UCNPs@SiO_2/g-C_3N_4, 3 wt%Ag/g-C_3N_4, and UCNPs@SiO_2@3wt%Ag/g-C_3N_4. The inset shows the absorption spectrum of UCNPs@SiO_2@Ag in water. (b) Plots of $(\alpha h\nu)^{1/2}$ *vs.* photon energy ($h\nu$).

absorption edge is due to the widening of the band gap energy of g-C_3N_4. As shown in Fig. 4b, the evaluated band gap energy of UCNPs@SiO_2/g-C_3N_4 is 2.82 eV, which is larger than that of g-C_3N_4 (2.70 eV). After assembly with UCNPs, the UCNPs@SiO_2/g-C_3N_4 presented a distinctive absorption band in the NIR region at about 980 nm, attributed to the $^2F_{7/2} \rightarrow {}^2F_{5/2}$ transition of the dopant Yb^{3+} ions in the UCNPs (Fig. S4 in ESI†).[40] After introducing Ag NPs into the composite or g-C_3N_4, an obvious red-shift of the absorption edge, and an enhanced absorption of g-C_3N_4 in the entire range from UV up to red were observed. The enhanced absorption in the visible light region is mainly attributed to the surface plasmon resonance (SPR) absorption of Ag NPs.[34] The red-shift of the absorption edge can be assigned to the narrowing of the band gap caused by the Ag nanoparticles. Ag, possessing a favorable Fermi level, can serve as a good electron acceptor. Therefore, the photogenerated electrons on the conduction band of g-C_3N_4 can quickly transfer to Ag NPs, resulting in a narrowing of the band gap of g-C_3N_4.[41] As shown in Fig. 4b, the estimated band gap energies for g-C_3N_4, Ag/g-C_3N_4 and UCNPs@SiO_2@Ag/g-C_3N_4 are 2.7, 2.53 and 2.53, respectively. The narrowing of the band gap is ascribed to the introduction of Ag nanoparticles. The optical absorption spectra for UCNPs@SiO_2@Ag/g-C_3N_4 samples with different contents of Ag were also investigated. As shown in Fig. S5,† the light absorption increases with increasing Ag content due to the SPR absorption of Ag nanoparticles. Meanwhile, the red-shift of the absorption edge increases with increasing Ag content due to the narrowing of the band gap energies arising from the Ag nanoparticles. The additional absorption band centered at 550 nm for the Ag/g-C_3N_4 spectra is assigned to the SPR absorption of Ag nanoparticles, which can also be seen in UCNPs@SiO_2@Ag/g-C_3N_4, but cannot be seen in g-C_3N_4 and UCNPs@SiO_2/g-C_3N_4 due to the absence of Ag nanoparticles. The extinction spectrum of UCNPs@SiO_2@Ag dispersed in water exhibits an absorption band in the wavelength range of 350–550 nm with a maximum absorption peak at 445 nm (Fig. 4a inset), corresponding to the SPR absorption of Ag NPs. Apparently, the SPR absorption, red-shift and enhanced absorption all over the spectral range, caused by Ag NPs, can greatly help the nanocomposite photocatalyst to harvest excitation light, leading to the much more efficient utilization of solar energy. This is a significant benefit to the improvement of the photocatalytic activity of the catalyst.

The migration, transfer and recombination of electron–hole pairs in the interfaces of composite photocatalysts have great influence on the photocatalytic activity. PL spectra were used to investigate the behavior of the electron–hole pairs.[6] Usually, a lower PL intensity of the photocatalyst indicates a lower recombination efficiency of electron–hole pairs.[17] The PL spectra of pure g-C_3N_4, 3wt%Ag/g-C_3N_4, and UCNPs@SiO_2@-*X*wt%Ag/g-C_3N_4 nanocomposites ($X = 0, 1, 3, 5, 10$) are shown in Fig. 5. The excitation wavelength of the PL spectra was set at 330 nm and all the samples display a similar band-to-band fluorescence emission, characteristic of g-C_3N_4. Two emission peaks located at 440 nm and 460 nm are observed in Fig. 5. The emission centered at 440 nm is caused by the transition between the δ* conduction band and the LP valence band,

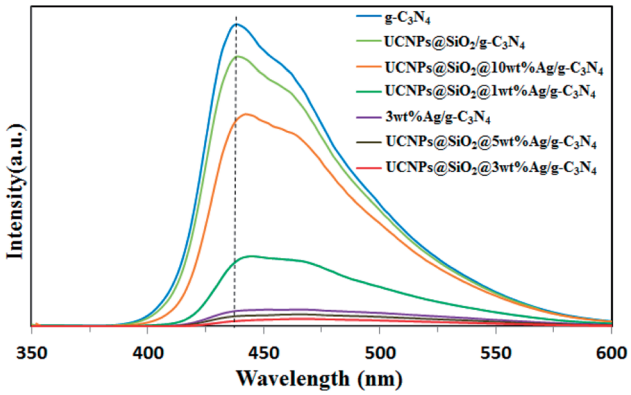

Fig. 5 Photoluminescence spectra of g-C_3N_4, 3wt%Ag/g-C_3N_4, and UCNPs@SiO_2@*X*wt%Ag/g-C_3N_4 (*X* = 0, 1, 3, 5, 10) under 330 nm excitation.

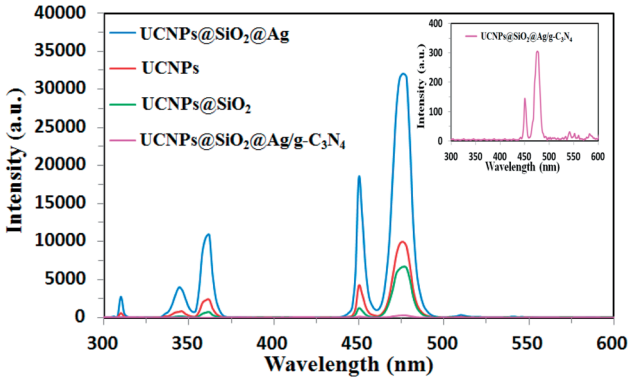

Fig. 6 UCL spectra of UCNPs, UCNPs@SiO_2, UCNPs@SiO_2@Ag, and UCNPs@SiO_2@3wt%Ag/g-C_3N_4 under 980 nm excitation. The inset is the enlarged view for UCNPs@SiO_2@3wt%Ag/g-C_3N_4.

which is related to the sp^2 C–N bond.[42] The emission band centered at 460 nm is attributed to the transition between the π* conduction band and the LP valance band.[42] It can be observed that g-C_3N_4 displays an intense fluorescence emission peak at 440 nm, while the PL intensity of other samples is much lower than that of g-C_3N_4. The strong fluorescence emission of g-C_3N_4 indicates a fast recombination of charge carriers, and the distinct fluorescence quenching of UCNPs@SiO_2@Ag/g-C_3N_4 indicates an efficient inhibition in the recombination of charge carriers. This might be due to the accelerated separation process of electron–hole pairs associated with the Ag NPs. It is well known that the noble metal Ag can act as an effective electron acceptor and transporter, trapping the photogenerated electrons, thereby improving the separation of electron–hole pairs and inhibiting their recombination.[43] In principle, the PL intensity of the nanocomposite would decrease with increasing Ag loading; however, the 3 wt% Ag loaded sample was found to display the lowest PL intensity. As the Ag loading increases to a certain degree, the Ag NPs aggregate on the surface and conversely work as recombination centers for charge carriers.[44] As for Ag/g-C_3N_4 and UCNPs@SiO_2@Ag/g-C_3N_4, the red-shift of the PL peak by Ag introduction reveals the narrowed bandgap relative to g-C_3N_4, which is in accord with the red-shift of the optical absorption edge, implying that the red-shift in the PL spectra is correlated to the red-shift of the optical absorption edge.

The UCNPs were employed to upconvert the NIR light into higher energy emissions in the UV and visible ranges, which are capable to excite the g-C_3N_4. As a crucial factor for the energy-transfer efficiency, the energy match between the emission of UCNPs and the absorption of g-C_3N_4 was investigated. The upconversion luminescence (UCL) spectra of the prepared samples under 980 nm excitation were measured and the results were shown in Fig. 6. The UCL intensities of the samples were measured at the same concentration of 2.0 mg mL^{-1} in ethanol. It can be seen that each of the samples shows a similar spectrum characteristic of the UCL of Tm^{3+}. Two blue-emission peaks at 476 and 450 nm, and two peaks at 361 and 345 nm in the UV region correspond to the $^1G_4 \rightarrow {}^3H_6$, $^1D_2 \rightarrow {}^3F_4$, $^1D_2 \rightarrow {}^3H_6$, and $^1I_6 \rightarrow {}^3F_4$ transitions of Tm^{3+}, respectively.[45,46] A very weak UV emission peak at 310 nm originated from the $^6P_{7/2} \rightarrow {}^8S_{7/2}$ transitions of Gd^{3+} ions.[47] As shown in Fig. 6, the emission intensities of the UCNPs are varied after coupling with SiO_2, Ag, or g-C_3N_4. The luminescence intensity of UCNPs@SiO_2 decreased to some extent in comparison to that of pure UCNPs due to the light scattering effects by the silica layer.[39] Though the presence of the SiO_2 shell leads to a small negative effect for the UCL intensity, the SiO_2 shell can serve as an interface for Ag decoration as well as an isolating layer to prevent fluorescence quenching induced by energy transfer from UCNPs to the metal Ag.[48,49] Moreover, this SiO_2 layer can protect the UCNPs from the photocatalytically-induced corrosion to prolong their lifetime.[50] As shown in Fig. 6, after loading Ag NPs, the UCL intensity of UCNPs@SiO_2 was significantly enhanced, which is attributed to the metal-enhanced fluorescence (MEF) of Ag NPs.[51] It is well known that noble metal nanoparticles can modulate the spectroscopic properties of nearby chromophores.[52] MEF arises from the interaction between the fluorophore and SPR of noble metal nanoparticles.[53] In our case, Ag NPs are located near the fluorophore of UCNPs. Induced by the SPR of Ag NPs, the local electric field in the proximity of Ag NPs drastically increases, which leads to the increase in the excitation rates of the UCNPs.[54] In addition, the interaction between fluorophore and SPR of Ag NPs can increase the emission rate as well as emission intensity of the fluorophore (UCNPs) by surface plasmon-coupled emission (SPCE).[22] As shown in Fig. 4 and 6, the SPR frequency of the Ag NPs overlaps well with the emission band of UCNPs, which permits an efficient SPCE. After the UCNPs@SiO_2@Ag is coupled with g-C_3N_4, the UCL intensity decreases remarkably, indicating that the upconverted emission is absorbed by g-C_3N_4, resulting from efficient energy transfer from UCNPs to the g-C_3N_4. As shown in Fig. 4 and 6, the absorbance band of g-C_3N_4 in the whole UV-Vis range overlaps with all the emission bands of UCNPs, indicating an energy match between the emission of the UCNPs and the absorption of the g-C_3N_4, which leads to an efficient energy transfer between the UCNPs and g-C_3N_4.

3.3. Photoelectrochemical measurements

Photoelectrochemical measurements, including transient photocurrent responses and electrochemical impedance spectroscopy (EIS) of the obtained g-C_3N_4, UCNPs@SiO_2/g-C_3N_4, Ag/g-C_3N_4, and UCNPs@SiO_2@Ag/g-C_3N_4 samples are shown in Fig. 7. The saturation photocurrent densities remain constant with the light on, and immediately drop to nearly zero once the light is switched off (Fig. 7a). Both photocurrent densities of the Ag/g-C_3N_4 and UCNPs@SiO_2/g-C_3N_4 are higher than that of pure g-C_3N_4. The increased photocurrent of Ag/g-C_3N_4 is ascribed to the Ag NPs, which facilitate the separation and prolong the lifetime of the photoinduced charge carries.[43] The increased photocurrent density of UCNPs@SiO_2/g-C_3N_4 as compared to the bare g-C_3N_4 is ascribed to the surface states of SiO_2, which is favorable for the separation and transfer of electron–hole pairs of g-C_3N_4.[55] The UCNPs@SiO_2@Ag/g-C_3N_4 composites present the highest photocurrent response intensity, which is about 4.2-fold higher than that of bare g-C_3N_4, indicating a lower recombination rate of charge carriers and faster photogenerated electron migration on g-C_3N_4. The increased photocurrent confirms that the incorporation of Ag NPs can facilitate the separation and prolong the lifetime of the photogenerated charge carriers, which is essential for the enhanced photocatalytic activity of g-C_3N_4. As mentioned above (in Section 3.2), the Ag NPs can act as effective electron acceptors and transporters, trapping the photogenerated electrons, thereby improving the separation of electron–hole pairs and prolonging the lifetime of the photogenerated charge carriers.[43] Moreover, due to the surface state of SiO_2, it can facilitate the separation and transfer of photogenerated electron–hole pairs due to the fact that photogenerated electrons on the CB of g-C_3N_4 tend to be transferred to impurity energy levels of SiO_2, prolonging the lifetime of the photogenerated charge carriers.[55] The almost unchanged photocurrent response during repeated light on–off cycles implies the excellent stability of the as-prepared photocatalysts. Electrochemical impedance spectroscopy (EIS) is another available method for studying the charge transfer efficiency and interface reaction ability.[56] Fig. 7b reveals the EIS Nyquist plots of the samples, which correspond to their charge transfer resistance. The smaller arc radius of the EIS Nyquist plot implies the lower impedance and faster interface charge transfer.[57] The UCNPs@SiO_2@Ag/g-C_3N_4 has the smallest arc radius of the EIS Nyquist plot, indicating that the UCNPs@SiO_2@Ag/g-C_3N_4 possesses the lowest impedance and fastest interface charge transfer. The results are in accord with those obtained by the photocurrent measurement.

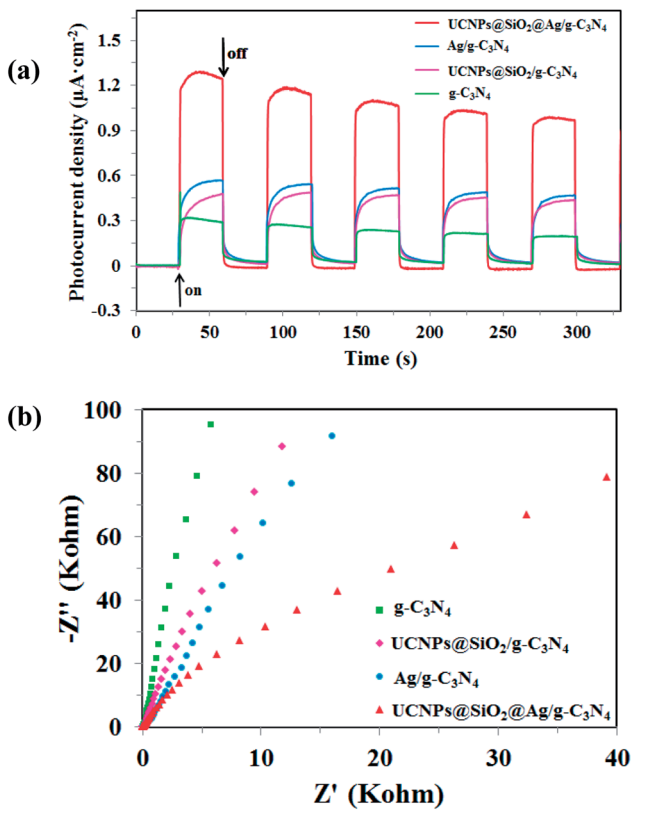

Fig. 7 (a) The transient photocurrent density response of the samples under 300 W Xe-lamp irradiation without cutoff filters for five on–off cycles at 0.2 V bias *vs.* Ag/AgCl. (b) EIS Nyquist plots of the electrochemical impedance spectroscopy of the samples in the dark.

3.4. Photocatalytic degradation of RhB

The photocatalytic properties of the as-prepared samples were evaluated firstly by the degradation of RhB under simulated solar light irradiation. Fig. 8 shows the absorbance spectra of RhB catalyzed by UCNPs@SiO_2@Ag/g-C_3N_4 under simulated solar light irradiation as a function of the irradiation time. The intensity of the characteristic peak of RhB, positioned at 554 nm, gradually decreased with the increase of light irradiation time, indicating the degradation of RhB upon simulated solar light irradiation. The photocatalytic activity of the nanocomposite was evaluated by calculating the time-dependent degradation ratio of the RhB with the controls of g-C_3N_4, Ag/g-C_3N_4, UCNPs@SiO_2/g-C_3N_4 and UCNPs@SiO_2@Ag. Fig. 9a shows the time profile of C/C_0 under stimulated solar light irradiation, where C is the concentration of RhB at the irradiation time and C_0 is the concentration at adsorption equilibrium with the photocatalyst before irradiation. As

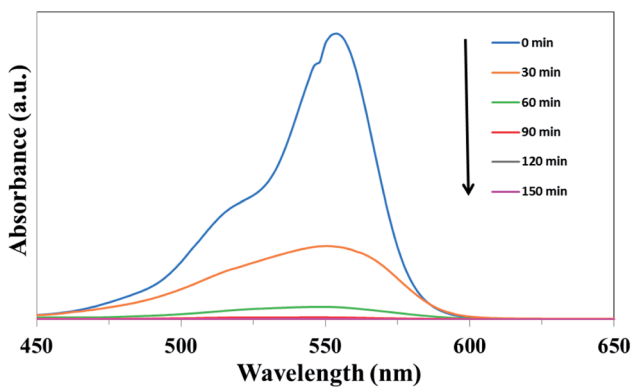

Fig. 8 Time-dependent absorption spectra for the photocatalytic degradation of RhB over UCNPs@SiO_2@Ag/g-C_3N_4 under simulated solar light irradiation.

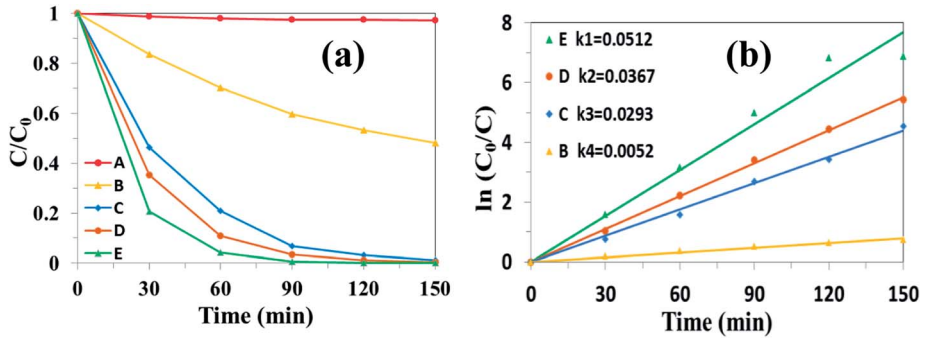

Fig. 9 (a) Photocatalytic degradation of RhB and (b) the kinetics study over different photocatalysts under simulated solar light irradiation: (A) UCNPs@SiO_2@Ag; (B) bulk g-C_3N_4; (C) UCNPs@SiO_2/g-C_3N_4; (D) Ag/g-C_3N_4; (E) UCNPs@SiO_2@3wt%Ag/g-C_3N_4.

shown in Fig. 9a, the photocatalytic efficiency of the UCNPs@SiO_2@Ag/g-C_3N_4 nanocomposite is obviously higher than that of the controls, where RhB is completely degraded in the presence of UCNPs@SiO_2@Ag/g-C_3N_4 after exposure under Xe lamp for 90 min. The rate constant of UCNPs@SiO_2@Ag/g-C_3N_4 is about 10 times higher than that of bare g-C_3N_4 (Fig. 9b). No significant degradation of RhB was observed in the presence of UCNPs@SiO_2@Ag, which implies that UCNPs or Ag cannot directly trigger the photocatalytic reaction, confirming the pivotal role of the g-C_3N_4 in the photocatalysis. After the g-C_3N_4 was integrated with UCNPs@SiO_2 nanoparticles, its photocatalytic activity was distinctly enhanced, which can be ascribed to the function of UCNPs. The UCNPs can absorb NIR light and convert it into UV and visible light, which are reabsorbed by g-C_3N_4. By utilizing the UCNPs, NIR light can be absorbed and harvested indirectly by g-C_3N_4 to broaden the absorption region and consequently enhance the photocatalytic activity of g-C_3N_4.[25] In addition, when the highly energetic UV photons produced by UCNPs are absorbed by the g-C_3N_4, it can drive the g-C_3N_4 to generate highly energetic charge carriers.[22] These highly energetic charge carriers possess high oxidation–reduction abilities, resulting in high catalytic activity.[23] As shown in Fig. 9b, the photocatalytic efficiency of UCNPs@SiO_2@Ag/g-C_3N_4 is higher than that of UCNPs@SiO_2/g-C_3N_4, and Ag/g-C_3N_4 is higher than that of g-C_3N_4, demonstrating that the Ag NPs present in the composite can result in the enhancement of photocatalytic activity. The Ag NPs play an important role in the composites. Firstly, the upconversion luminescence of UCNPs is enhanced by the presence of Ag NPs on the outer shell layer of UCNPs due to its metal-enhanced fluorescence effect,[51] which can make better use of UCNPs as an upconversion luminescent center in the composite. Secondly, Ag NPs serve as effective electron acceptors and transporters,[58] which can trap the photogenerated electrons of g-C_3N_4, thereby improving the separation of electron–hole pairs and inhibiting their recombination.[59] Finally, the Ag NPs act as visible light harvesting components *via* the excitation of the SPR to enhance the light absorption ability of the composite.[39,60] Notably, the photocatalytic degradation activity of the as-prepared nanocomposite is also higher than the various UCNPs-modified photocatalysts reported previously (Table S1 in ESI†).[25,27,28]

Considering that the amount of Ag loading may be an important factor in the photocatalysis, the dependence of the degradation efficiency of RhB on the amount of Ag loading (0–10 wt%) was studied further. As shown in Fig. S6 (ESI),† with the increase in Ag content, the photocatalytic efficiency of UCNPs@SiO_2@Ag/g-C_3N_4 increases and reaches a maximum value for the 3 wt% Ag loaded sample. The rate constant of UCNPs@SiO_2@3wt%Ag/g-C_3N_4 is about 2 times higher than that of UCNPs@SiO_2/g-C_3N_4. Further increase in the Ag NPs loading (>3 wt%) causes a reduction in the photocatalytic efficiency. The defects introduced by excessive Ag NPs at the interface between Ag NPs and g-C_3N_4 can act as the recombination centers for charge carriers,[6] which account for the presence of the optimal Ag loading amount.

The possible mechanism of photodegradation of RhB in the presence of the UCNPs@SiO_2@Ag/g-C_3N_4 photocatalyst under simulated solar light irradiation is depicted in Fig. S7 (ESI).† To further confirm the contribution of the upconversion materials, a test of the photocatalytic degradation of RhB under NIR irradiation was performed. The obtained results are shown in Fig. S8.† Similar to the results obtained under simulated solar irradiation, the highest photocatalytic efficiency was also obtained by UCNPs@SiO_2@3wt%Ag/g-C_3N_4, which is much higher than that of the controls. Since g-C_3N_4 or Ag NPs cannot be directly excited by the NIR light, no significant degradation of RhB was observed in the presence of UCNPs@SiO_2@Ag, g-C_3N_4, and Ag/g-C_3N_4. These results further confirm the pivotal role of UCNPs for photocatalysis.

3.5. Detection of active species in the photocatalysis

For the in-depth investigation of the photodegradation mechanism of RhB, the radical capture experiments were performed. Generally, superoxide radicals ($\cdot O_2^-$), hydroxyl radicals ($\cdot$OH), and photogenerated holes (h^+) are the acknowledged active species in the photocatalytic degradation of organic molecules.[61] Therefore, trapping experiments were performed to identify the active species involved in this reaction system by using three different types of scavengers over the UCNPs@SiO_2@Ag/g-C_3N_4 sample, namely, BQ (a quencher of $\cdot O_2^-$), *t*-BuOH (a quencher of $\cdot$OH), and Na_2EDTA (a quencher of h^+). Fig. 10 shows the photodegradation ratios of RhB in the presence of different scavengers under simulated solar light

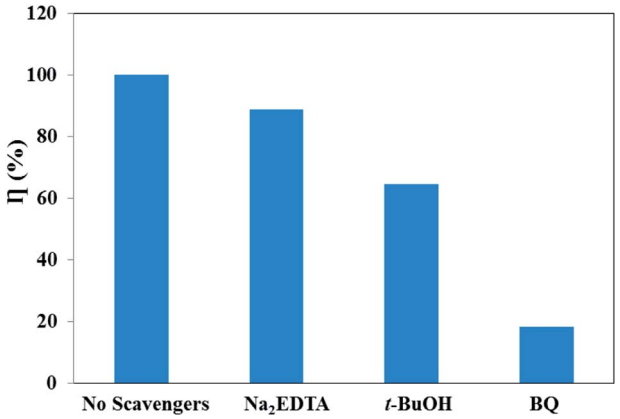

Fig. 10 Photodegradation ratios of RhB over UCNPs@SiO_2@3wt%Ag/g-C_3N_4 in the presence of different scavengers under simulated solar light irradiation.

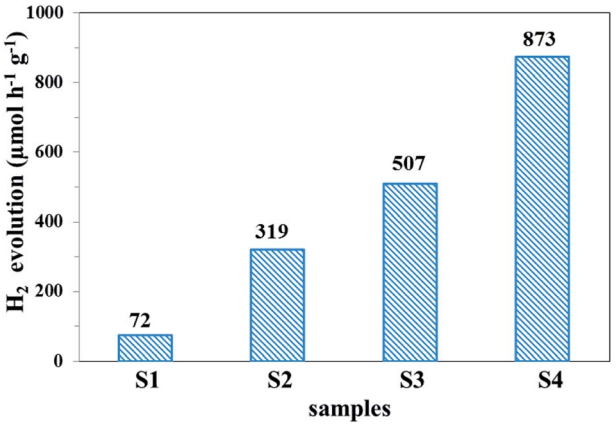

Fig. 11 Hydrogen evolution rates of (S1) g-C_3N_4, (S2) UCNPs@SiO_2/g-C_3N_4, (S3) 3wt%Ag/g-C_3N_4, and (S4) UCNPs@SiO_2@3wt%Ag/g-C_3N_4 under simulated solar light irradiation (irradiation time = 5 h).

irradiation for 90 min. It was found that ~100% RhB degradation was achieved without adding scavengers. However, the degradation ratio decreased significantly to 18.3% with the addition of BQ (1 mM), indicating that $\cdot O_2^-$ is the major reactive species. Meanwhile, the addition of *t*-BuOH (1 mM) and Na_2EDTA (1 mM) as scavengers was also found to inhibit the degradation ratio to 64.5% and 88.7%, respectively, which indicates that ·OH plays a more important role than h^+ in the reaction. Therefore, the influence of the active species in the process of RhB photodegradation follows the trend $\cdot O_2^-$ > ·OH > h^+.

3.6. Photocatalytic hydrogen evolution and stability

The photocatalytic hydrogen evolution ability of the samples was evaluated under simulated solar light irradiation, which is shown in Fig. 11. Compared with pure g-C_3N_4, the UCNPs@SiO_2/g-C_3N_4 and 3wt%Ag/g-C_3N_4 nanocomposites showed higher hydrogen evolution rates of 319 and 507 μmol h^{-1} g^{-1}, respectively. The highest photocatalytic hydrogen evolution rate of 873 μmol h^{-1} g^{-1} was realized with the UCNPs@SiO_2@3wt%Ag/g-C_3N_4 nanocomposite, which was about 12 times higher than that of bare g-C_3N_4 (72 μmol h^{-1} g^{-1}). The improved photocatalytic activity is mainly ascribed to the synergistic effect of UCNPs and Ag NPs, which results in a broad light-response range of g-C_3N_4 as well as the fast separation and slow recombination of the photoinduced electron–hole pairs. Interestingly, the photocatalytic H_2 production activity of the UCNPs@SiO_2@3wt%Ag/g-C_3N_4 is also higher than other previously reported photocatalysts involving upconversion materials (Table S2 in ESI†).[62,63] In the recycling test of the UCNPs@SiO_2@3wt%Ag/g-C_3N_4 nanocomposite for photocatalytic hydrogen evolution (Fig. 12), the hydrogen evolved per hour hardly decreased during each cycle. Moreover, in the five successive cycles, the catalytic effect of each period remained almost consistent, indicating that the photocatalyst is reusable and possesses excellent stability. The high performance and stability of the as-synthesized photocatalysts are beneficial to the large-scale application of photocatalysis in the field of energy and environment.

3.7. Photocatalytic mechanisms of hydrogen evolution

To better understand the photocatalytic process, the possible mechanism of hydrogen evolution in the presence of the UCNPs@SiO_2@Ag/g-C_3N_4 photocatalyst under simulated solar light irradiation is depicted in Fig. 13. The g-C_3N_4 is an n-type semiconductor with the redox potential of the conduction band (CB) and the valence band (VB) located at −1.3 eV and +1.4 eV *vs.* NHE,[64] respectively. The substrate material of g-C_3N_4 can harvest UV and visible light shorter than 460 nm due to its intrinsic properties. The high penetrability of the NIR from the solar light is absorbed by the UCNPs of $NaLuF_4$:Gd,Yb,Tm@$NaLuF_4$:Gd,Yb to emit UV and visible light, which can subsequently be absorbed by g-C_3N_4. After absorbing the solar and upconverted light, the excited g-C_3N_4 generates electron–hole pairs. The Ag NPs with the Fermi level at +0.4 eV *vs.* NHE[65] can act as an excellent electron reservoir that favors the

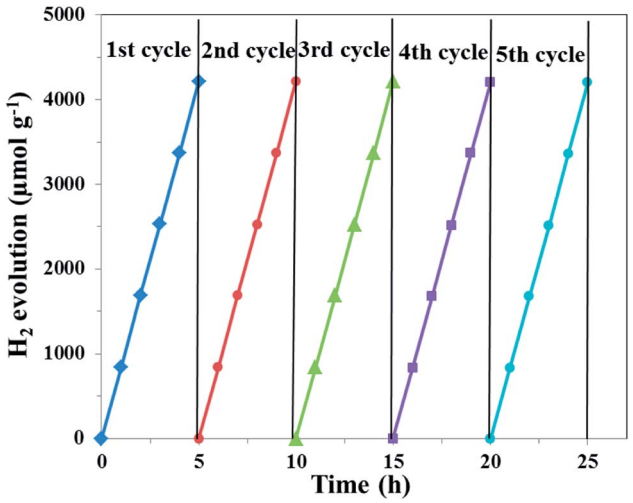

Fig. 12 Recycling test of the obtained UCNPs@SiO_2@3wt%Ag/g-C_3N_4 nanocomposite for photocatalytic hydrogen evolution in five successive cycling reactions. The duration of simulated solar light exposure in each cycle was 5 h (irradiation time = 25 h).

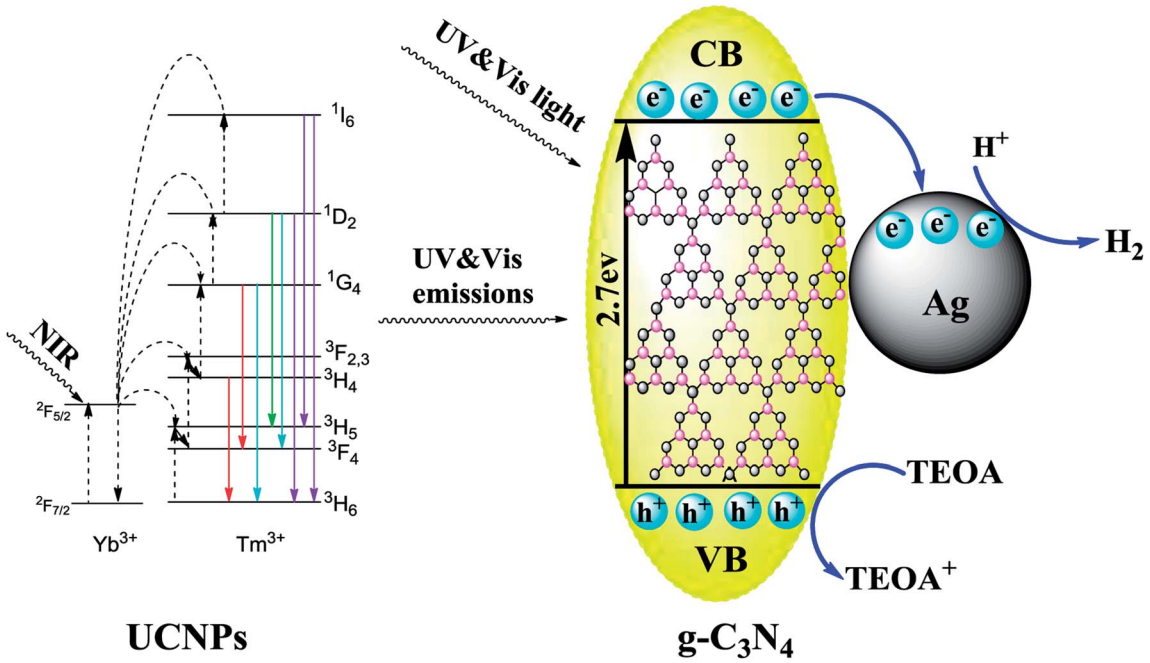

Fig. 13 Schematic of the photocatalytic mechanism in the UCNPs@SiO_2@Ag/g-C_3N_4 photocatalysts under simulated solar light irradiation.

electron transfer from the VB of g-C_3N_4 to the surface of Ag NPs. The electrons accumulate on Ag NPs to create a Schottky barrier that inhibits the recombination of the photogenerated electron–hole pairs. The strong local electromagnetic field induced by the SPR effect of Ag NPs can enhance the captured electron energy and transfer rate so that the electrons can react more easily with H^+ for H_2 production. Simultaneously, most of the holes are consumed by TEOA, promoting the separation of photogenerated charge carriers and producing more H^+ to participate in the following reaction. Moreover, the SPR effect strengthens the sunlight harvesting capacity of the photocatalysts, resulting in the boosted generation rate of photogenerated charge carriers.

4. Conclusions

In this work, both upconversion and plasmonic effects were introduced into photocatalysis to gain a largely broadened light response range and fast separation of photoinduced electron–hole pairs. The UCNPs@SiO_2@Ag/g-C_3N_4 composite photocatalysts with different Ag content were successfully designed and synthesized for the first time by subtly integrating UCNPs, Ag NPs and g-C_3N_4 nanosheets into a single nanoarchitecture. The as-prepared photocatalysts successfully used solar energy and restrained the recombination of charge carriers, showing exceptional activity in the photocatalytic degradation of RhB and hydrogen production as compared with plain g-C_3N_4. The effects of Ag loading on the photocatalytic properties of the catalyst were investigated and the photocatalytic mechanism was suggested. The present work offers a feasible strategy for designing and synthesizing high-performance photocatalysts by utilizing upconversion and plasmon-enhanced effects. The novel photocatalyst may have the potential for application in the removal of pollutants and hydrogen production in the future.

Conflicts of interest

There are no conflicts to declare.

Acknowledgements

The authors acknowledge the National Natural Science Foundation of China (No. 21271126), Program for Innovative Research Team in University (No. IRT 13078), and National 973 Program (No. 2010CB933901).

References

1 K. X. Li, Z. X. Zeng, L. S. Yan, S. L. Luo, X. B. Luo, M. X. Huo and Y. H. Guo, *Appl. Catal., B*, 2015, **165**, 428–437.
2 Q. Li, N. Zhang, Y. Yang, G. Z. Wang and D. H. L. Ng, *Langmuir*, 2014, **30**, 8965–8972.
3 M. Tahir, C. B. Cao, F. K. Butt, S. Butt, F. Idrees, Z. Ali, I. Aslam, M. Tanveer, A. Mahmood and N. Mahmood, *CrystEngComm*, 2014, **16**, 1825–1830.
4 K. Srinivasu, B. Modak and S. K. Ghosh, *J. Phys. Chem. C*, 2014, **118**, 26479–26484.
5 D. J. Martin, P. J. T. Reardon, S. J. A. Moniz and J. W. Tang, *J. Am. Chem. Soc.*, 2014, **136**, 12568–12571.
6 Z. Zhu, Z. Y. Lu, D. D. Wang, X. Tang, Y. S. Yan, W. D. Shi, Y. S. Wang, N. L. Gao, X. Yao and H. J. Dong, *Appl. Catal., B*, 2016, **182**, 115–122.

7 M. Koelsch, S. Cassaignon, C. T. T. Minh, J. F. Guillemoles and J. P. Jolivet, *Thin Solid Films*, 2004, **451**, 86–92.
8 H. Wang, X. Z. Yuan, H. Wang, X. H. Chen, Z. B. Wu, L. B. Jiang, W. P. Xiong and G. M. Zeng, *Appl. Catal., B*, 2016, **193**, 36–46.
9 H. Wang, X. Z. Yuan, Y. Wu, G. M. Zeng, X. H. Chen, L. J. Leng and H. Li, *Appl. Catal., B*, 2015, **174**, 445–454.
10 A. Zada, M. Humayun, F. Raziq, X. L. Zhang, Y. Qu, L. L. Bai, C. L. Qin, L. Q. Jing and H. G. Fu, *Adv. Energy Mater.*, 2016, **6**, 1601190.
11 C. Ye, J. X. Li, Z. J. Li, X. B. Li, X. B. Fan, L. P. Zhang, B. Chen, C. H. Tung and L. Z. Wu, *ACS Catal.*, 2015, **5**, 6973–6979.
12 Y. Wang, J. S. Zhang, X. C. Wang, M. Antonietti and H. R. Li, *Angew. Chem., Int. Ed.*, 2010, **49**, 3356–3359.
13 D. D. Zheng, C. Y. Pang, Y. X. Liu and X. C. Wang, *Chem. Commun.*, 2015, **51**, 9706–9709.
14 Y. Shiraishi, Y. Kofuji, S. Kanazawa, H. Sakamoto, S. Ichikawa, S. Tanaka and T. Hirai, *Chem. Commun.*, 2014, **50**, 15255–15258.
15 T. Xiong, W. L. Cen, Y. X. Zhang and F. Dong, *ACS Catal.*, 2016, **6**, 2462–2472.
16 D. Lu, G. K. Zhang and Z. Wan, *Appl. Surf. Sci.*, 2015, **358**, 223–230.
17 J. Y. Qin, J. P. Huo, P. Y. Zhang, J. Zeng, T. T. Wang and H. P. Zeng, *Nanoscale*, 2016, **8**, 2249–2259.
18 X. Xin, J. Y. Lang, T. T. Wang, Y. G. Su, Y. X. Zhao and X. J. Wang, *Appl. Catal., B*, 2016, **181**, 197–209.
19 M. T. Song, Y. H. Wu, X. J. Wang, M. Q. Liu and Y. G. Su, *J. Colloid Interface Sci.*, 2018, **529**, 375–384.
20 G. Liu, Y. N. Zhao, C. H. Sun, F. Li, G. Q. Lu and H. M. Cheng, *Angew. Chem., Int. Ed.*, 2008, **47**, 4516–4520.
21 S. Lee, I. Cho and Y. Sohn, *J. Nanosci. Nanotechnol.*, 2015, **15**, 8362–8369.
22 C. C. Wang, K. L. Song, Y. Feng, D. G. Yin, J. Ouyang, B. Liu, X. Z. Cao, L. Zhang, Y. L. Han and M. H. Wu, *RSC Adv.*, 2014, **4**, 39118–39125.
23 Y. N. Tang, W. H. Di, X. S. Zhai, R. Y. Yang and W. P. Qin, *ACS Catal.*, 2013, **3**, 405–412.
24 X. F. Li, H. Ren, Z. J. Zou, J. J. Sun, J. Y. Wang and Z. H. Liu, *Chem. Commun.*, 2016, **52**, 453–456.
25 Q. Z. Zhang, J. J. Deng, Z. H. Xu, M. Chaker and D. L. Ma, *ACS Catal.*, 2017, **7**, 6225–6234.
26 Z. H. Xu, M. Quintanilla, F. Vetrone, A. O. Govorov, M. Chaker and D. L. Ma, *Adv. Funct. Mater.*, 2015, **25**, 2950–2960.
27 D. G. Yin, L. Zhang, X. Z. Cao, Z. W. Chen, J. X. Tang, Y. M. Liu, T. T. Zhang and M. H. Wu, *Dalton Trans.*, 2016, **45**, 1467–1475.
28 D. G. Yin, F. F. Zhao, L. Zhang, X. Y. Zhang, Y. M. Liu, T. T. Zhang, C. L. Wu, D. W. Chen and Z. W. Chen, *RSC Adv.*, 2016, **6**, 103795–103802.
29 F. Wang, T. T. Wang, J. Y. Lang, Y. G. Su and X. J. Wang, *J. Mol. Catal. A: Chem.*, 2017, **426**, 52–59.
30 T. T. Wang, J. Y. Lang, Y. J. Zhao, Y. G. Su, Y. X. Zhao and X. J. Wang, *CrystEngComm*, 2015, **17**, 6651–6660.
31 D. J. Martin, K. P. Qiu, S. A. Shevlin, A. D. Handoko, X. W. Chen, Z. X. Guo and J. W. Tang, *Angew. Chem., Int. Ed.*, 2014, **53**, 9240–9245.
32 P. Niu, L. L. Zhang, G. Liu and H. M. Cheng, *Adv. Funct. Mater.*, 2012, **22**, 4763–4770.
33 F. F. Zhao, D. G. Yin, C. L. Wu, B. Q. Liu, T. Chen, M. T. Guo, K. X. Huang, Z. W. Chen and Y. Zhang, *Dalton Trans.*, 2017, **46**, 16180–16189.
34 P. Y. Yuan, Y. H. Lee, M. K. Gnanasammandhan, Z. P. Guan, Y. Zhang and Q. H. Xu, *Nanoscale*, 2012, **4**, 5132–5137.
35 J. W. Lee, M. R. Othman, Y. Eom, T. G. Lee, W. S. Kim and J. Kim, *Microporous Mesoporous Mater.*, 2008, **116**, 561–568.
36 Y. Y. Kang, Y. Q. Yang, L. C. Yin, X. D. Kang, L. Z. Wang, G. Liu and H. M. Cheng, *Adv. Mater.*, 2016, **28**, 6471–6477.
37 D. G. Yin, X. Z. Cao, L. Zhang, J. X. Tang, W. F. Huang, Y. L. Han and M. H. Wu, *Dalton Trans.*, 2015, **44**, 11147–11154.
38 D. G. Yin, C. C. Wang, J. Ouyang, X. Y. Zhang, Y. Feng, K. L. Song, B. Liu, X. Z. Cao, L. Zhang, H. Y. Lin and M. H. Wu, *ACS Appl. Mater. Interfaces*, 2014, **6**, 18480–18488.
39 P. Zhao, Y. H. Zhu, X. L. Yang, X. Jiang, J. H. Shen and C. Z. Li, *J. Mater. Chem. A*, 2014, **2**, 16523–16530.
40 S. Heer, K. Kömpe, H. U. Güdel and M. Haase, *Adv. Mater.*, 2004, **16**, 2102–2105.
41 Y. B. Wang, X. Zhao, D. Cao, Y. Wang and Y. F. Zhu, *Appl. Catal., B*, 2017, **211**, 79–88.
42 B. B. Wang, Q. J. Cheng, L. H. Wang, K. Zheng and K. Ostrikov, *Carbon*, 2012, **50**, 3561–3571.
43 H. H. Yin, K. Yu and C. Q. Song, *ACS Appl. Mater. Interfaces*, 2014, **6**, 14851–14860.
44 E. Z. Liu, L. M. Kang, Y. H. Yang, T. Sun, X. Y. Hu, C. J. Zhu, H. C. Liu, Q. P. Wang, X. H. Li and J. Fan, *Nanotechnology*, 2014, **25**, 165401.
45 G. Chen, J. Damasco, H. Qiu, W. Shao, T. Y. Ohulchanskyy, R. R. Valiev, X. Wu, G. Han, Y. Wang, C. Yang, H. Ågren and P. N. Prasad, *Nano Lett.*, 2015, **15**, 7400–7407.
46 S. H. Tang, J. N. Wang, C. X. Yang, L. X. Dong, D. L. Kong and X. P. Yan, *Nanoscale*, 2014, **6**, 8037–8044.
47 Y. Chen, X. H. Yan, Q. Liu and X. F. Wang, *J. Alloys Compd.*, 2013, **562**, 99–105.
48 F. Zhang, G. B. Braun, Y. F. Shi, Y. C. Zhang, X. H. Sun, N. O. Reich, D. Y. Zhao and G. Stucky, *J. Am. Chem. Soc.*, 2010, **132**, 2850–2851.
49 D. M. Cheng and Q. H. Xu, *Chem. Commun.*, 2007, 248–250.
50 J. Kummerlen, A. Leitner, H. Brunner, F. R. Aussenegg and A. Wokaun, *Mol. Phys.*, 1993, **80**, 1031–1046.
51 A. Camplon, A. R. Gallo, C. B. Harris, H. J. Robota and P. M. Whitmore, *Chem. Phys. Lett.*, 1980, **73**, 447–450.
52 H. J. Chen, T. Ming, L. Zhao, F. Wang, L. D. Sun, J. F. Wang and C. H. Yan, *Nano Today*, 2010, **5**, 494–505.
53 S. Eustis and M. A. El-Sayed, *Chem. Soc. Rev.*, 2006, **35**, 209–217.
54 W. Wang, W. J. Huang, Y. R. Ni, C. H. Lu and Z. Z. Xu, *ACS Appl. Mater. Interfaces*, 2013, **6**, 340–348.
55 Q. Hao, X. X. Niu, C. S. Nie, S. M. Hao, W. Zou, J. M. Ge, D. M. Chen and W. Q. Yao, *Phys. Chem. Chem. Phys.*, 2016, **18**, 31410–31418.

56 F. He, G. Chen, Y. G. Yu, S. Hao, Y. S. Zhou and Y. Zheng, *ACS Appl. Mater. Interfaces*, 2014, **6**, 7171–7179.
57 X. F. Chang, S. B. Wang, Q. Qi, M. A. Gondal, S. G. Rashid, D. Y. Yang, M. A. Dastageer, K. Shen, Q. Y. Xu and P. Wang, *Appl. Catal., B*, 2015, **176**, 201–211.
58 H. Chen, F. Gao, R. He and D. X. Cui, *J. Colloid Interface Sci.*, 2007, **315**, 158–163.
59 D. G. Yin, L. Zhang, B. H. Liu and M. H. Wu, *J. Nanosci. Nanotechnol.*, 2012, **12**, 2248–2253.
60 D. G. Yin, B. H. Liu, L. Zhang and M. H. Wu, *J. Biomed. Nanotechnol.*, 2012, **8**, 458–464.
61 K. C. Christoforidis, T. Montini, E. Bontempi, S. Zafeiratos, J. J. D. Jaén and P. Fornasiero, *Appl. Catal., B*, 2016, **187**, 171–180.
62 W. Gao, W. Y. Zhang and G. X. Lu, *Appl. Catal., B*, 2017, **212**, 23–31.
63 J. W. Shi, J. H. Ye, L. J. Ma, S. X. Ouyang, D. W. Jing and L. J. Guo, *Chem.–Eur. J.*, 2012, **18**, 7543–7551.
64 M. Xu, L. Han and S. J. Dong, *ACS Appl. Mater. Interfaces*, 2013, **5**, 12533–12540.
65 Y. X. Yang, Y. N. Guo, F. Y. Liu, X. Yuan, Y. H. Guo, S. Q. Zhang, W. Guo and M. X. Huo, *Appl. Catal., B*, 2013, **142**, 828–837.